Imidazolium-Based Anion Exchange Membranes for Alkaline Anion Fuel Cells: (2) Elucidation of the Ionic Structure and its Impact on Conducting Properties

Kimio Yoshimura,[1] Yue Zhao,[1,*] Shin Hasegawa,[1] Akihiro Hiroki,[1] Yoshihiro Kishiyama,[2] Hideyuki Shishitani,[2] Susumu Yamaguchi,[2] Hirohisa Tanaka,[2] Satoshi Koizumi,[3] Marie-Sousai Appavou,[4] Aurel Radulescu,[4] Dieter Richter,[5] Yasunari Maekawa[1,*]

[1]*Department of Advanced Functional Materials Research, Takasaki Advanced Radiation Research Institute, National Institutes for Quantum and Radiological Science and Technology (QST), Watanuki-machi 1233, Takasaki, Gunma, 370-1292, Japan*

[2]*Daihatsu Motor Co., Ltd., Ryuo Gamo, Shiga 520-2593, Japan*

[3]*Department of Engineering, Ibaraki University, Hitachi 316-8511, Japan*

[4]*Forschungszentrum Jülich GmbH, Jülich Centre for Neutron Science @ MLZ, Lichtenbergstraße 1, D-85747 Garching, Germany*

[5]*Jülich Centre for Neutron Science & Institute for Complex Systems, Forschungszentrum Jülich GmbH, D-52425 Jülich, Germany*

*To whom all correspondence should be addressed: Yue Zhao (zhao.yue@qst.go.jp); Yasunari Maekawa (maekawa.yasunari@qst.go.jp);

ABSTRACT: In our previous study (*Soft Matter* 2016, 12, 1567), the relationship between the morphology and properties of graft-type imidazolium-based anion exchange membranes (AEMs) was revealed, in that the semi-crystalline features of the polymer matrix maintain its mechanical properties and the formation of interconnected hydrophilic domains promotes the membrane conductivity. Here, we report the novel ionic structure of the same graft-type AEMs with different grafting degrees, analyzed using a small-angle X-ray scattering method under different relative humidity (RH) conditions. The characteristic "ionomer peak" with a corresponding correlation distance of approximately 1.0 nm was observed at RH < 80%. This distance is much smaller than the literature-reported mean distance between two ionic clusters, but close to the Bjerrum length of water. Since the representative number of water molecules per cation, n_w, was small, we proposed that dissociated ion-pairs are distributed in the hydrophilic domains (ion-channels). At RH < 80%, ion-channels are disconnected, however in liquid water, they are well-connected as evidenced by the sharp increase in n_w. The disconnected ion-channels even under relatively high RH conditions should be a substantial factor for the low power generation efficiency of AEM-type fuel cells.

I. Introduction

In recent years, anion exchange membranes (AEMs) have been treated as an alternative to proton-exchange membranes (PEMs) in energy conversion devices such as fuel cells, electrolyzers, and redox flow batteries. These membranes have potential advantages for the direct oxidation of hydrogen-containing fuels, improving the performance of liquid fuels, and high reaction kinetics at the electrode under basic conditions, allowing for the use of inexpensive non-precious metal catalysts in such systems.[1–7] Compared to the plenty studies on PEMs such as Nafion,[8–18] neither the molecular design nor the property understanding are sufficient for developing AEMs capable of practical fuel cell applications.[19] Therefore, it is crucial to thoroughly study the microstructures of current AEMs, to explain ion and water transport in the membranes, the alkaline stability, and mechanical properties.

One promising method to fabricate AEMs is by a radiation grafting technique. There have been intensive reports including our previous studies[20–23] on this method being successfully applied to the preparation of AEMs or PEMs, where graft polymers containing ion-conducting groups are grafted onto fluorinated polymer films such as cross-linked polytetrafluoroethylene (cPTFE), poly(ethylene-co-tetrafluoroethylene) (ETFE), and poly(vinylidene fluoride) (PVDF) or fully aromatic hydrocarbon polymers such as poly(ether ether ketone).[21–30] This technique allows for the introduction of large amounts of ion-conducting groups into the membranes to promote ion conductivity. Among them, ETFE is regarded as the most promising base material because of its good mechanical strength, thermal/chemical stability, and feasibility for graft polymerization.

To improve the alkaline stability of the cationic head-groups, systems involving multiple *N* atoms, *i.e.* heterocyclic imidazolium systems, have been evaluated with the desire of developing alkali stable and conductive AEMs.[3-5] It is known that polyvinylimidazolium cations of the graft-polymers in AEMs are subjected to β-elimination because of very acidic protons at β-carbons from two imidazolium nitrogen atoms in adjacent *N*-vinylimidazolium

units in the graft-polymers and hydrolytic ring opening degradation reactions, so that the anion conductivity of the AEM reduces severely in alkaline solution.[5, 31] For suppressing β-elimination, we have reported in our previous study[31] that the introduction of copolymers of imidazolium and styrene units to the graft-polymer chains as a spacer can reduce the sequence of adjacent vinylimidazolium units. In that work, β-elimination in imidazolium-based AEMs with and without copolymerization of styrene were systematically studied and we concluded that copolymerization suppresses β-elimination efficiently, and the copolymer-type AEMs exhibit higher alkaline stability than homo-polyvinylimidazolium type AEMs. Another dominant degradation pathway for imidazolium cations is the nucleophilic addition-elimination at the C-2 atom position on the imidazolium ring. Many theoretical and experimental works, on how to prevent this type of degradation in presence of hydroxide ions, have been published. [5, 31, 32] For instance, Long *et al* found the introduction of substitutions at C-2 position has a significant positive impact on calculated degradation energy barriers based on the density functional theory.[32] Most lately, Varcoe *et al* reviewed the up-to-date perspectives on the use of AEMs,[5] and enumerated many experimental proofs that the replacement of the protons at the C-2 position by methyl or butyl groups increases the stability of the imidazolium group. For suppressing ring-opening hydrolysis, we also introduced the protecting methyl group at 2-posion of imidazolium ring to prevent the hydroxide attack.

Based upon the procedures above, we successfully prepared a new graft-type of AEMs composed of poly(dimethyl-vinylimidazole-co-styrene) graft copolymer chains with a molar ratio of 65:35, grafted onto ETFE films via a radiation-induced grafting method (Scheme 1). In our previous study, we found that a specific such type of AEM with ion exchange capacity (IEC) of 1.82 mmol/g and grafting degree (GD) of 91%, defined as AEM91 herewith, had both high conductivity and relatively high alkaline stability, both of which are required for fuel cell applications.[20] We investigated the grafting, alkylation and swelling effects on the morphology of these AEMs, and elucidated the interplay between the morphology and properties using a

contrast variation SANS method. Our study revealed that the crystalline lamellae and crystallites originating from the pristine ETFE material are conserved in the AEMs, hence their good mechanical properties. When AEM91 is equilibrated in water, inter-connected hydrophilic domains are formed, leading to good ion conductivity. We concluded that the micro-structure of AEM91 in water can be characterized as a three-phase system: phase 1) is the crystalline ETFE phase, which offers good mechanical properties; phase 2) is the hydrophobic amorphous ETFE phase, which allows the matrix to create conducting regions; and phase 3) is the hydrophilic phase, which promotes conductivity. We further confirmed that the hydrophilic phase is composed of whole graft chains and water, and the correlation length of concentration fluctuations of the grafts is ~2.5 nm. Since ion transport occurs in the hydrophilic domains, we denote these domains as ion-channels hereafter. Our previous study was the first attempt to elucidate the hierarchical structure in the graft-type AEMs with relatively high GD in a quantitative manner.[20]

It is generally accepted that a common feature among ion-containing polymers such as PEMs or AEMs is the presence of ionic clusters,[33–39] because dipole-dipole interactions between the ion pairs along the polymer chain cause aggregation or clustering of ion-rich moieties within the nonpolar polymer matrix. The standard methodology for detecting the presence of ionic clusters is small-angle X-ray scattering (SAXS) and neutron scattering (SANS) to observe the so-called "ionomer peak".[21–23, 33–39] The spherical morphology of the ionic clusters was first proposed for Nafion by Hsu and Gierke,[34] and for sulfonated polystyrene by Yarusso and Cooper.[38] The mean distance between two ionic clusters, $d_{cluster}$, has been reported as between 1.8 and 6.0 nm for a wide variety of charged polymers, including polymers with both strong and weak ionic groups, polymers neutralized with different counter-ions, dry and hydrated polymers, crystalline and amorphous polymers, random and block copolymers.[33–39] To our surprise, the ionomer peak was not plainly observed in our previous work.[20] Thus, the ionic structure of these AEMs is still in question, especially at length scales < 2 nm, the most

important length scale for conductive properties. The fact that no clear ionomer peak was observed by SANS at a q-range below 4.0 nm^{-1} may be due to the cluster-free distribution of dissociated negative and positive ion pairs. Thus, we can only extract the concentration fluctuation of the ion-containing grafts in the measured q-range of the SANS instrument, but not the correlation length of the dissociated ion-pairs, which is expected to be close to the Bjerrum length of water (0.7 nm).[40] If this hypothesis is true, an ionomer peak originating from dissociated ion-pairs might be observed at a higher q-range when using a proper method with good scattering contrast.

Therefore, in this report, we introduce a SAXS method to extend the observed scale into the high q-range up to 13 nm^{-1}. With this extension, the < 2 nm structure of ion-channels in these AEMs can be elucidated, the structure of which determines the conductivity. The correlations among the conductivity, hydration level and morphology of a series of AEMs with grafting degree of 30%, 48%, 91% and 108% are discussed. Since X-rays are more sensitive to heavy elements, the scattering contrast between ionic groups and the polymer matrix can be efficiently enhanced by the exchange of the counter-ion from bicarbonate used in the previous SANS measurement with chloride ($N^+HCO_3^- \rightarrow N^+Cl^-$). All AEMs used in this study are in the chloride form.

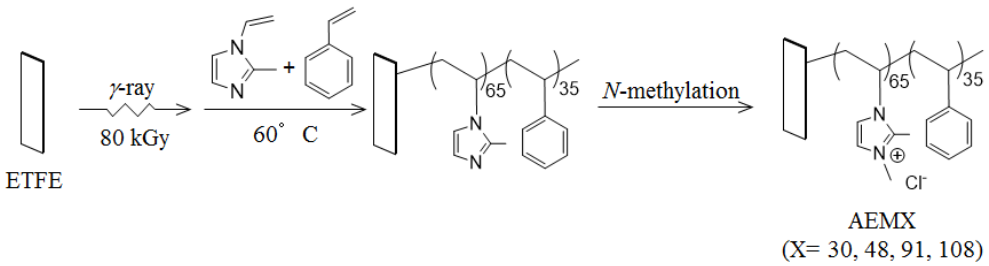

Scheme 1 Preparation procedures for AEMs by radiation-induced grafting of 2-methyl-1-vinylimidazole and styrene into ETFE films, followed by *N*-alkylation with methyliodide, and the molecular structure of the AEMs used in this study.

II. Experimental

II-1, Sample preparation and characterization. AEMs (AEM30, AEM48, and AEM108)

were prepared by radiation-induced grafting of 2-methyl-1-vinylimidazole and styrene into ETFE films (Asahi Glass Co. Ltd., thickness = 50 μm, mass density (d_{ETFE}) = 1.75 g/cm^3, crystallinity (X_c) = 0.32) followed by *N*-alkylation with methyliodide, as described in detail in the previous paper for AEM91.[20]

The GD of these AEMs can be estimated using Eq. (1)

$$GD(\%) = \frac{W_g - W_0}{W_0} \times 100\% \qquad (1)$$

where W_0 and W_g are the weights of the membranes before and after grafting in the dry state, respectively. The graft-polymerization for 2, 5, and 24 h yielded copolymer-grafted ETFE films with GDs of 30%, 48%, and 108% respectively (Table 1). The molar ratio of 2-methyl-1-vinylimidazole to styrene units in the grafts for all AEMs was set to ~65:35, which has been verified by gravimetric measurements of grafted membranes, given that the N-alkylation proceeds in a quantitative manner. The mass density of the grafts (d_{graft}) can be calculated as ~0.98 g/cm^3 on the basis of the reported mass densities of polystyrene and poly(*N*-vinylimidazole) homo-polymers being 1.05 and 0.95 g/cm^3, respectively.

The IECs were determined using a standard back-titration method. The dried AEMs were immersed in 15 mL of 0.1 N HCl solution for 24 h. The solution was then titrated with 0.1 N NaOH solution using an automatic titrator (HIRANUMA COM-555). The IEC value was calculated as IEC = $[(V_{ref}\text{-}V_{mem})\times C/W_{dry}] \times 10^{-1}$, where V_{ref} and V_{mem} are the volumes of the NaOH consumed in the titration without and with membranes, respectively. C is the concentration of NaOH solution, and W_{dry} is the mass of the dry AEMs.[20, 31, 41] The grafted ETFE films with GDs of 30%, 48%, and 108% were converted to AEMs with IEC values of 0.95, 1.56, and 2.32 mmol/g, respectively as listed in Table 1.

AMEs with different hydration levels were obtained by equilibrating the dry AEMs at a specific relative humidity (RH) in a humidity controlled chamber or in liquid water at room temperature. Water-uptake (WU) of an AEM under specific conditions was calculated by the

weight measurements as

$$\mathrm{WU}(\%) = \frac{W_{wet} - W_{dry}}{W_{dry}} \times 100\% \qquad (2)$$

where W_{wet} and W_{dry} represent the weights of the AEMs in the hydrated and dry states, respectively. To measure RH dependence of WU, an AEM was placed in the chamber for 2 h. After the membrane was taken out, it was placed into a plastic bag and sealed to prevent vapor absorption or desorption and quickly weighed on a microbalance. To measure the WU in water, the membrane was completely hydrated in water and lightly wiped with Kimwipes to remove the excess water on the surface before weighing.

In this study, WU of AEMs is estimated from H_2O-swollen membranes, where the mass density of water (d_w) is 1.0 g/cm^3. Thus, the volume fraction of grafts, ϕ_{graft}, can be estimated as a function of GD and WU as

$$\phi_{graft} = \frac{GD/d_{graft}}{\frac{1}{d_{ETFE}} + \frac{GD}{d_{graft}} + \frac{WU(1+GD)}{d_w}} \qquad (3)$$

where WU = 0 for the dry AEMs. WU and ϕ_{graft} values for each AEM at different hydration conditions are summarized in Table 1.

II-2. Electrochemical Impedance Spectroscopy. The membrane in-plane anionic conductivity was measured by an AC impedance method using a LCR HiTESTER 3522-50 at a frequency of 100 Hz. A membrane was placed between two platinum electrodes, and the conductivity in the plane direction of the membrane was measured by impedance spectroscopy at a fixed temperature. To measure the RH dependence of the conductivity, a membrane was placed and equilibrated in an ESPEC-2K temperature/humidity control chamber wherein the RH range was 30–80% at the prescribed temperature.[20, 31] The ionic conductivity σ (mS/cm) of a given membrane can be calculated as $\sigma = L/(S \times R) \times 10^3$, where L (cm) is the distance between two electrodes, S (cm^2) is the cross-section area of the membrane obtained by multiplying the membrane thickness with the membrane width, and R (Ω) is the membrane resistance.

It is generally accepted that if ions are completely dissociated in a solution, the temperature

dependence of the ionic conductivity follows Arrhenius behavior, as

$$\sigma = \sigma_0 \exp(\frac{-E_a}{RT}) \qquad (4)$$

where σ_0 is the pre-exponential factor, E_a is the apparent activation energy (J/mol) for ion transport, R is the gas constant (8.314 J/mol·K), and T is the absolute temperature (K), respectively. Thus E_a can be determined from the slope of the linear plot of $\ln\sigma$ vs $1/T$ as

$$Ea = -slope \times R \qquad (5)$$

II-3. Small-angle X-ray Scattering (SAXS) measurement. SAXS measurements were performed on SAXS spectrometers (NANOPIX, Rigaku co., Japan) in QST, Takasaki, Japan. The X-rays (Cu-Kα, wavelength = 0.154 nm) were generated by a rotating anode generator operated at 40 kV and 30 mA, and focused by two-dimensional confocal mirrors. The AEMs were stacked to a thickness of ~300 μm, and placed in the stainless sample holder with a 5 mm-diameter pinhole for X-rays to pass through. The sample holder was placed in a polycarbonate chamber (HUM-1F, Rigaku Co., Japan), which can precisely control the experimental environment at a specific %RH (10–80%) and temperature (RT–90 °C). The sample chamber was located between the X-ray source and the detector (PILATUS 100K, Dectris, Baden, Switzerland). The scattering patterns were circularly averaged to obtain scattering intensity profiles as a function of scattering vector q, which is defined by $q = (4\pi/\lambda)\sin(\theta/2)$, with λ and θ being the wavelength of the X-ray and the scattering angles, respectively; q ranges from 0.08 to 13 nm^{-1}. The obtained SAXS scattering intensity profiles $I(q)$, were corrected for the sample adsorption, instrument background, detector sensitivity, and scattering from empty cell, and finally calibrated to an absolute scale (cm^{-1}) using glassy carbon provided by Argonne National Laboratory.[42]

III. Results and Discussion

III-1, Effect of hydration conditions on the conducting properties of AEMs. Prior to the structural analysis of the AEMs using SAXS, we quantitatively investigated the dependence of

the hydration conditions on conductivity (σ) and water uptake (WU), which are important properties of AEMs directly related to fuel cell power generation and durability.

Figures 1(a) and 1(b) show σ and WU of AEM91 as functions of RH, respectively. σ gradually increases from 0.1 to 4.3 mS/cm as RH changes from 30 to 80%, and notably jumps to 21 mS/cm when AEM91 is equilibrated in liquid water. WU also shows the same tendency to increase steadily from 5.9 to 17.5% at this RH range, and then increases greatly to 60.2% in water. It is known that the incorporation of water in the AEM results to the swelling of the membrane, and the swelling ratio (SR) is generally defined by the change of the membrane area between the dry and wet AEMs as $SR = \frac{A_{wet}-A_{dry}}{A_{dry}} \times 100\%$, with A_{wet} and A_{dry} being the area of the dry and wet AEM at different RH or in water, respectively. SR values of AEM91 are listed in Table 1. Similar to the change in WU, SR also shows a steady increase at RH < 80%, and then a great increase in water. Such a sharp change in σ and WU in this instance was also observed in other types of AEMs,[5,43-45] and similar to that of PEMs such as Nafion◯,R,[45–47] suggesting that for the graft-type AEMs, the so-called Schroeder's paradox phenomenon observed in PEMs also exist.[47]

In order to verify the significant changes in σ and WU of the AEM at 80% RH and in liquid water, we measured σ and WU of AEMs with different GDs in both states, plotting them as functions of GD in Figures 2(a) and 2(b), respectively. Commonly, σ and WU of all AEMs in water are 3–4 times higher than those at 80% RH. We believe that this big increment of σ and WU can be attributed to the structural change of the ion channels. However, since the polymer matrix is glassy materials, rearrangements of the grafts are unlikely, so that the structural change is mainly due to the swelling and connection of ion channels.

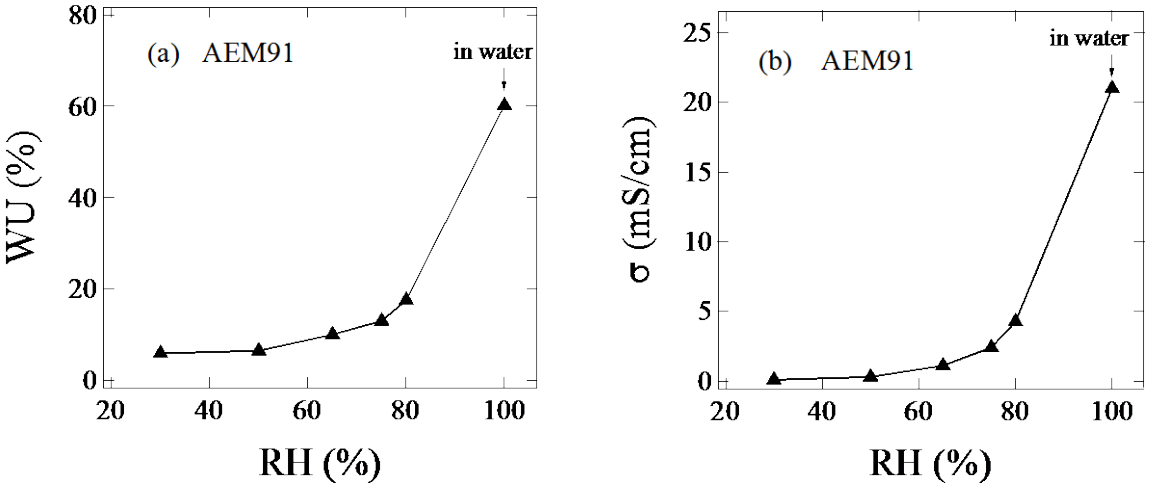

Figure 1 RH dependence of (a) WU and (b) σ of AEM91 at room temperature.

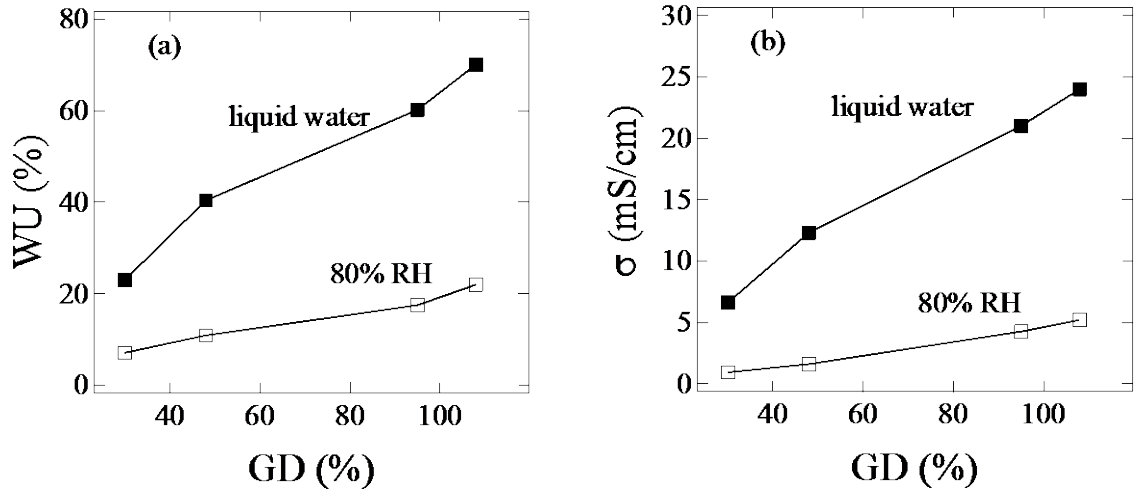

Figure 2 GD dependence of (a) WU and (b) σ of AEMs equilibrated at 80% RH and in liquid water at room temperature.

III-2, Morphological changes of AEM91 under various RH conditions. We investigated the ionic structure of ion-channels in AEM91 at different RH and GDs by using a SAXS method. SAXS profiles of AEM91 equilibrated at 0% (dry), 30%, 50%, 65% and 80% RH at room temperature are plotted as functions of q in Figure 3. According to the scattering features, SAXS profiles can be classified into two q-regions: Region 1 at $q < 2$ nm^{-1}, related to the crystalline lamellar structure and Region 2 at $q > 2$ nm^{-1}, related to the ionic structure of ion channels. In

the following sections, we shall discuss the morphologies in these two regions.

Region 1: A broad scattering maximum around $q_1 \sim 0.21$ nm^{-1} was observed for AEM91 at all RH, representing the typical first-order lamellar peak conserved from the pristine ETFE film. The details of this peak have been reported in the literature including our previous studies.[20,23,48] SAXS profiles around this peak were found to overlap one another, indicating little change in the lamellar structure. In order to precisely determine the periodicity of the crystalline domains, we considered the application of the small angle Lorentz correction or the calculation of the invariant argument, $I(q)q^2$. The effect of this data analysis on $I(q)q^2$ with q is shown in Figure S1 (Supporting Information). The position of q_1 for each profile is determined and the corresponding lamellar d-spacing ($d_1=2\pi/q_1$) is plotted as a function of RH in Figure 4(a). For comparison, d_1 is ~34 nm for AEM91 equilibrated in water, which was estimated from previous SANS measurement and is also plotted here.[20] It shows that d_1 is steady at RH < 80%, and then greatly increases in water, consistent with the changes of WU as shown in Figure 1(a), confirming that the incorporation of water in the amorphous domains is the key factor for the expansion of the lamellar spacing in AEMs.

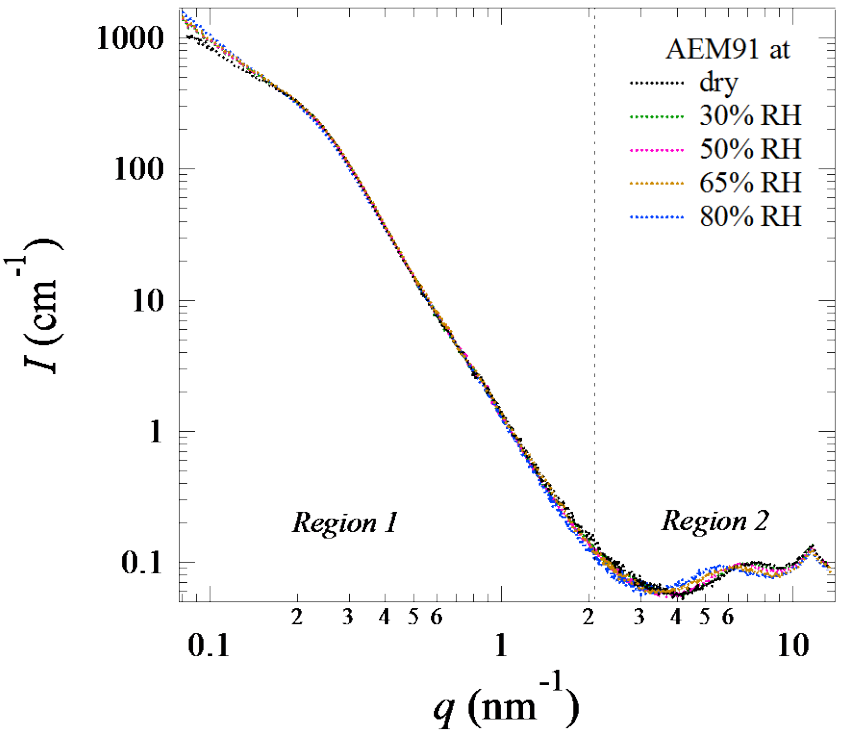

Figure 3 SAXS profiles measured for AEM91 equilibrated at RH of 0% (black), 30% (green), 50% (pink), 65% (yellow) and 80% (blue) at room temperature. The vertical broken line indicates the boundary between Region 1 and Region 2.

Region 2: The SAXS profiles in Figure 3 clearly show two scattering maxima in Region 2. One maximum is attributed to the scattering from the amorphous ETFE halo observed at $q \sim 12$ nm^{-1},[48] the position of which is not affected by the hydration level, but its intensity decreases slightly with increasing RH. This is because the introduction of water decreases the volume fraction of the ETFE amorphous regions in the sample. The other maximum appears at 5.0–7.0 nm^{-1}, which shifts towards low-q range with increasing RH, and represents correlations among the so-called "ionic particles", being either dissociated ion-pairs or ionic clusters.

The distribution of ionic particles can be fitted well by a Gaussian distribution function, where the scattering intensity around the peak, $I_{\text{ion}}(q)$, can be expressed as

$$I_{ion}(q) = I_{m,ion}G(q) + I_c \qquad (6)$$

where $I_{\text{m,ion}}$ is the peak height, $G(q)$ is the Gaussian distribution function about the ion peak around $q_{\text{m,ion}}$ as given by $G(q) = \frac{1}{(2\pi)^{1/2}\sigma_q}\exp[-(q - q_{m,ion})^2/(2{\sigma_q}^2)]$ (with σ_q being the standard deviation of $q_{\text{m,ion}}$), and I_c is the baseline scattering intensity.[49] We fitted the scattering profiles at q = 4–9 nm^{-1} with the theoretical scattering function numerically calculated from Eq. (6) and the fitting curves can be found in Figure S2 in the supporting information with red lines; in this way, $I_{\text{m,ion}}$ and $q_{\text{m,ion}}$ were evaluated. The mean distance between two ionic particles, d_{ion} (= $2\pi/q_{\text{m,ion}}$), is estimated accordingly, and plotted as a function of RH in Figure 4(b) and also summarized in Table 1. It shows that d_{ion} is ~0.9 nm in the dry state, increases gradually with increasing RH and reaches ~1.1 nm at RH ~ 80%. We believe that d_{ion} will further increase in the RH range of 80–100%, though the corresponding SAXS data is not available in the current experimental setup. However, our previous study concluded a correlation length of ~2.5 nm for

the concentration fluctuation of grafts in AEM91 equilibrated in water. Since grafts distribute in the hydrophilic domains, this correlation length is regarded as the mean distance between two ion-channels. For comparison, the correlation length of ~2.5 nm in water is marked in Figure 4(b).

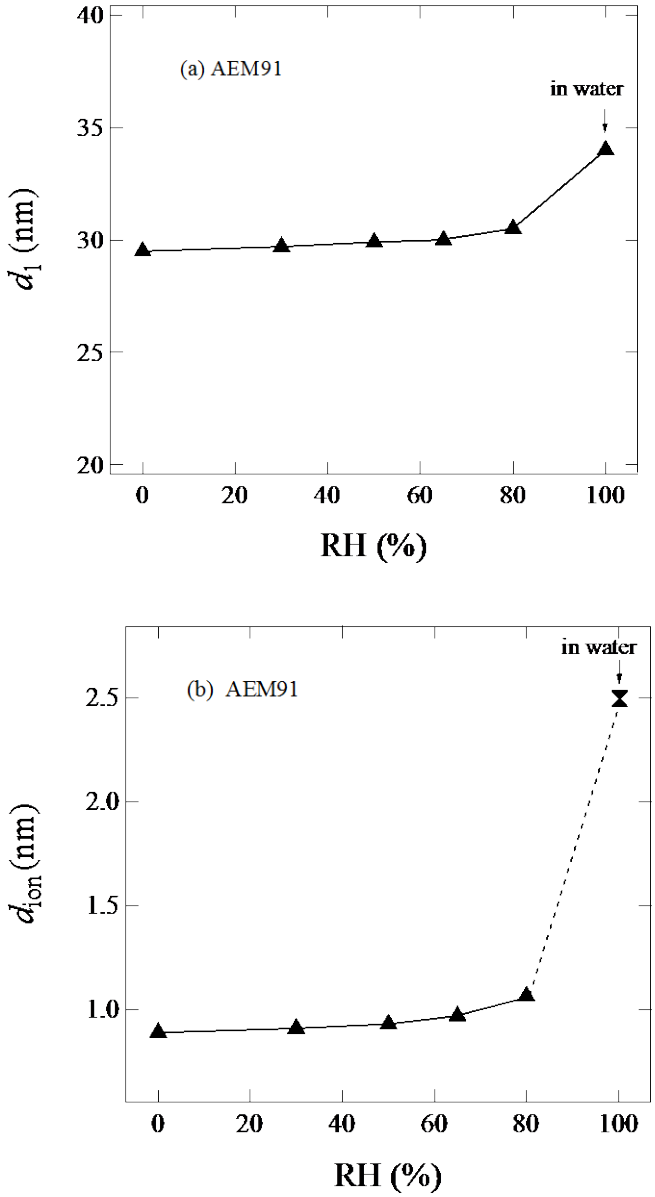

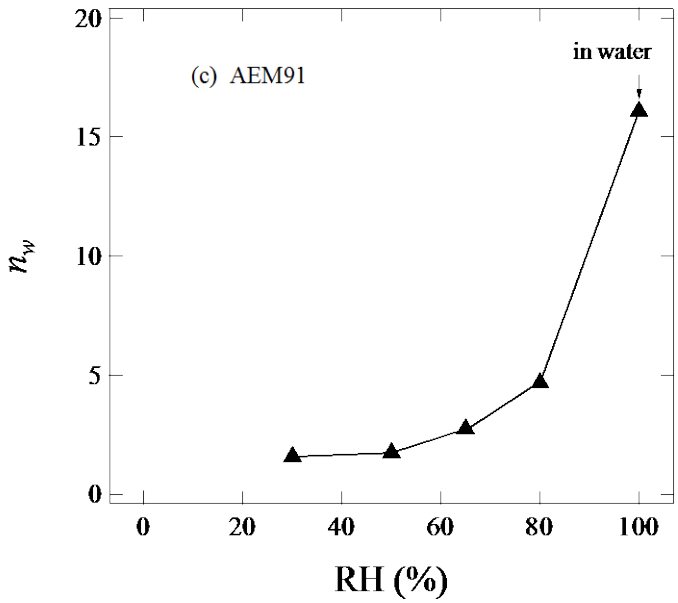

Figure 4 RH dependence of (a) d_1, (b) d_{ion}, and (c) n_w of AEM91. Note that the points in water are marked by arrows, where data in (a) and (b) are taken from the SANS results in Ref. 20, and the one in (b) is the correlation length between two ion channels.

Proposed ionic structural model for AEM91. d_{ion} (0.9–1.1 nm) of AEM91 at RH < 80% is much smaller than the literature-reported mean distance between two ionic clusters (1.8–6.0 nm),[33-39] likely indicating that ionic particles in AEM91 are dissociated "ion-pairs" but not "ionic clusters". Generally, the hydration level of a given AEM can be quantitatively defined in terms of the number of water molecules per cation (n_w), calculated as

$$n_w = \frac{WU/M_{H2O}}{IEC/1000} \qquad (7)$$

where M_{H2O} is the molecular weight of H_2O (18 g/mol). The resultant n_w of AEM91 is plotted as a function of RH in Figure 4(c). As RH increases from 0 to 80%, n_w steadily increases from ~1.6 to ~4.7, which is smaller than the commonly accepted hydration value for Cl^- anions in solution (n_w = 6).[50] Such a small n_w at RH < 80% may suggest that ion-channels are disconnected; however, n_w rapidly increases to ~16 in water, indicating that well-connected ion-

channels are formed. This tendency is the same as that of WU as shown in Figure 1(a), because Eq. (7) shows that n_w is proportional to WU for a given AEM with the same IEC value.

Considering the above discussion, we propose that the dissociated ion-pairs are distributed in ion-channels as illustrated in Figure 5. When an insufficient amount of water is present (RH < 80%), ion-channels are disconnected as shown in Figure 5(a), making anion transport difficult and making the conductivity low. When there is sufficient water present, the ion-channels are well-connected as shown in Figure 5(b), promoting anion transport in the connected channels and improving the conductivity.

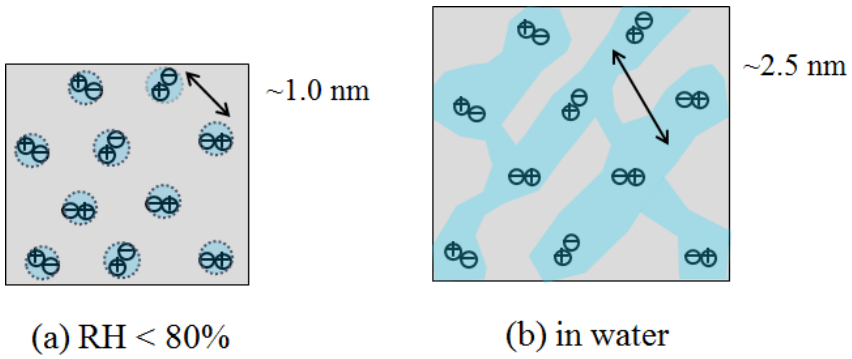

Figure 5 Schematic illustrations of the ionic structure of ion channels in AEM91 (a) at RH < 80% and (b) in water.

The proposed ionic structure of AEM91 in Figure 5 is supported by the Arrhenius behavior (temperature dependence) of the anion conductivity.[51–53] Conductivities of AEM91 at 50%, 65%, 80% RH and in water as a function of temperature from 25–80 °C are shown in Figure S3 in the supporting information. At each RH, two slightly different linear Arrhenius behaviors with a transition temperature of ~60 °C are observed. Thus, the activation energy of anion transport for conductivity can be estimated by Eq. (5) over two temperature ranges: T-range 1 at 25–60 °C and T-range 2 at 60–80 °C. The resultant E_a values are plotted in Figure 6 and listed in Table 1. E_a in T-range 1 is slightly larger than that in T-range 2, likely because the mobility

of the polymer grafts slightly increases at T > 60 °C. It should be emphasized that the Arrhenius dependence of the AEM91 conductivity on temperature implies that the segmental motion of the grafts is not a crucial phenomenon for the long-range anion-transfer mechanism. The negligible polymer segmental motion is likely caused by the completely random distribution of imidazolium and styrene segments on the graft chain. As a consequence, the ionic groups are well spaced out by the styrene groups, which in turn form the dissociated "ion-pairs".

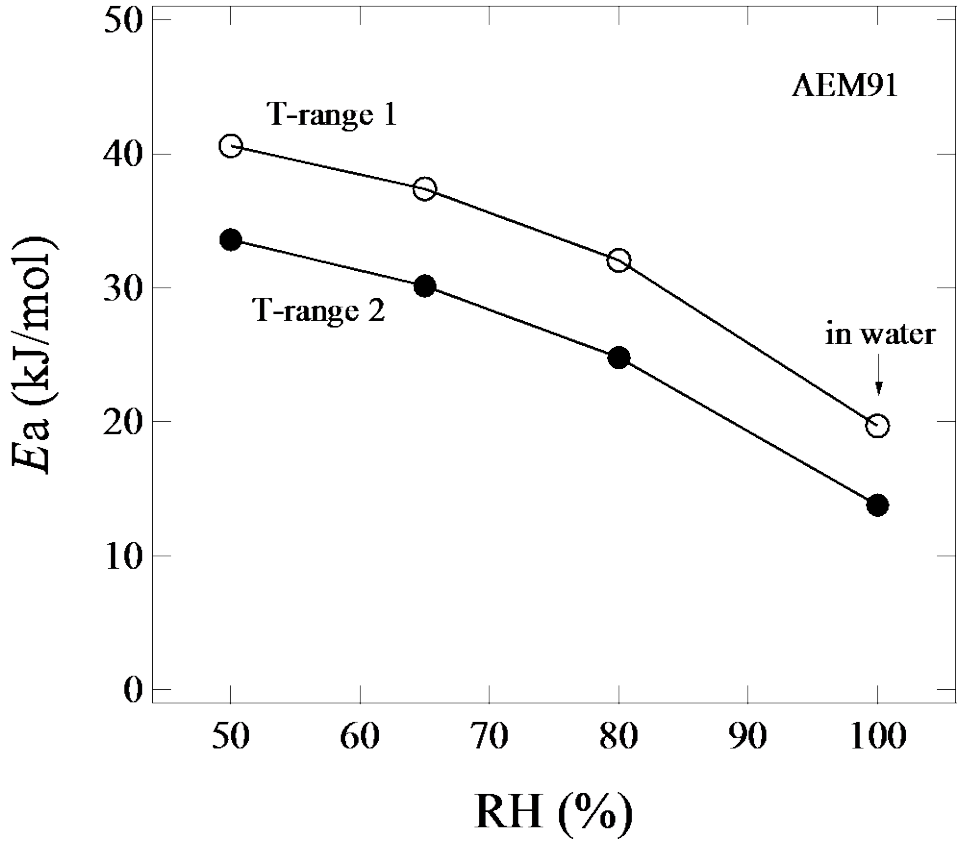

Figure 6 RH dependence of E_a for AEM91.

E_a also decreases with increasing RH, because the number of water molecules available to solvate the Cl^- anions increases, and thus the movement of anions is promoted and E_a is accordingly suppressed. Note that σ of AEM91 equilibrated at 30% RH is very low and almost independent of temperature, indicating that at such a low RH, there is insufficient water to solvate Cl^- anions. Therefore, similar to the dry state case, most of the anions are bound, or formed into tight ion-pair with each other in the grafts, and unable to participate in the

conduction process.[54–58]

It is interesting to note that σ is proportional to n_w/d_{ion} at RH < 80%, as shown in Figure 7. Roughly, by linear extrapolation of the experimental plots toward zero, we can obtain a n_w/d_{ion} threshold value of 1.78 for σ = 0, which may represent the onset of anion transport. The existence of this threshold for anion transport further evidences the disconnected ion-channels at low hydration levels.

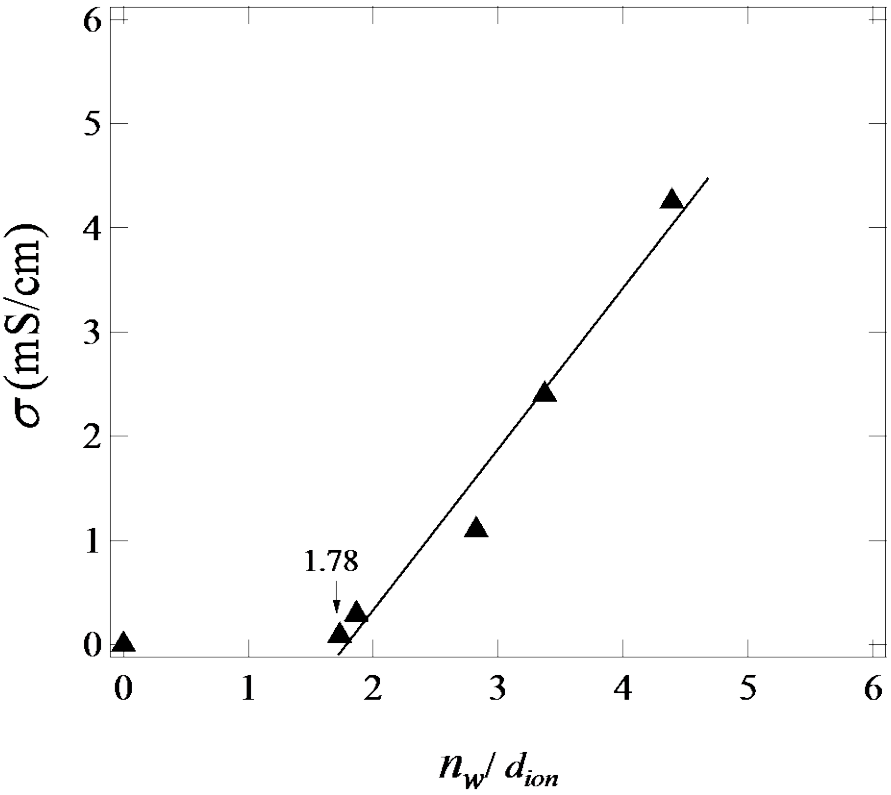

Figure 7 σ as a function of n_w/d_{ion} for AEM91 at RH < 80%. The threshold value of n_w/d_{ion} (~1.78) for σ = 0 is marked by the arrow.

III-3, Morphological change of AEMs with various GDs. SAXS profiles of AEMs with different GDs at a dry state are shown in Figure 8. Figure 8(a) shows the overall scattering profiles of AEMs (in absolute units) obtained at room temperature, some of which overlap with one another. The profiles in Figure 8(b) were vertically shifted to avoid overlapping of the profiles in order to illuminate the details of each profile. According to the definition of two *q*-

regions in section III-1.1, we shall separately discuss the morphology in these two regions.

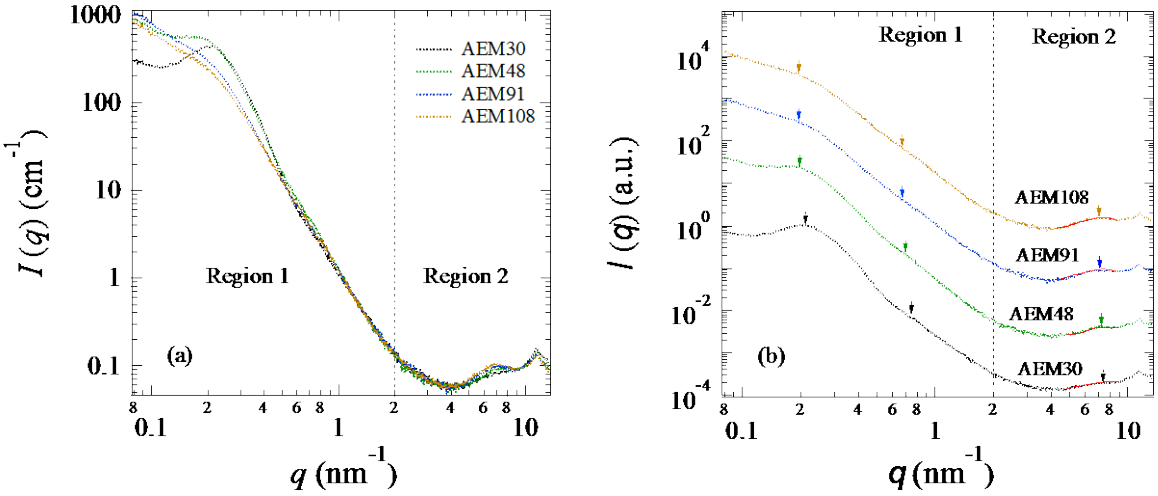

Figure 8 SAXS profiles measured for AEMs with different GDs in the dry state at room temperature (a) in absolute intensity units and (b) in arbitrary units derived by vertically shifting profiles shown in part (a) to avoid overlapping. The best-fitted theoretical profile across the ion-related peak from Eq. (6) for each measured scattering profile is shown using red lines. The vertical broken lines in both parts indicate the boundary between Region 1 and Region 2.

Region 1. A scattering maximum around 0.2–0.25 nm^{-1} was observed for all AEMs, representing typical lamellar peak. The SAXS profile of AEM30, which has the lowest GD, shows the most profound scattering peak at q_1 = 0.24 nm^{-1}, corresponding to the lamellar structure with a *d*-spacing ($d_1=2\pi/q_1$) of 26.2 nm. The shoulder-like third-order Bragg peak is observed at $3q_1$, further confirming the formation of the ordered lamellar microdomain structures. With increasing GD, the peak position of q_1 shifts to lower values, indicating an increased lamellar *d*–spacing due to the incorporation of grafts in the amorphous ETFE domains. Additionally, flattening and broadening of the peak is observed, which is in agreement with the previous SANS findings due to the fact that the incorporation of graft chains perturbs the

arrangement of the lamellar crystals and decreases the overall crystallinity.[20]

SAXS profiles for all AEMs equilibrated at 80% RH (shown in Figures S4 (a) and (b) in the supporting information) were very similar to those at a dry state in Figure 8, except for the left-shift of the scattering maximum at q_1. We applied the small angle Lorentz correction to determine the peak position q_1 for AEMs at both dry and 80% RH conditions; plots of $I(q)q^2$ vs q at both conditions are shown in Figure S5 (a) and (b) respectively. The resultant first-order peak at q_1 and the third-order peak at $3q_1$ for all profiles were marked by arrows in Figure 8(b) and Figure S4(b). It should be noted that the long-range order of lamellar patterns is believed to exist in the original ETFE base film, though the higher-order peak, *i.e.* third-order peak was not clearly observed,[23] due to the fact that the scattering contrast (difference in the electron density) between amorphous and crystalline ETFE phases in the substrate is too small for the same molecular structures but the only slightly different molecular volume. It is conceivable that the incorporation of grafts or water in the amorphous ETFE phase affects the long-range interactions in two ways: (a) It increases the scattering contrast between the crystalline ETFE phase and the amorphous phase, so that the third-order peak is enhanced and becomes more obvious; (b) It decreases the overall crystallinity and increases the heterogeneity of crystallites, so that the long-range ordering of lamellae is destabilized, consequently the third-order peak is weakened. The counter-balance between these two factors finally determines the appearance of the third-order peak. If the effect (a) outweighs the effect (b), the third-order peak becomes obvious: this may be the case observed for AEMs with low GDs. If the effect (b) outweighs the effect (a), the third-order peak becomes vague: this may be the case observed for AEMs with high GDs.

The lamellar *d*-spacing, estimated on the basis of q_1, was plotted as a function of GD for AEMs at both dry and 80% RH conditions in Figure 9(a). d_1 increases with the increase of GD up to 48%, and then changes steadily with further increases in GD. This tendency was also observed by a SANS method in our previous study[20] and in ETFE- and PTFE-based PEMs.[21–

[23] At the early stage of graft polymerization, most graft chains were created within the lamellar stacks, so that d_1 increases accordingly, while at the later stage of polymerization, graft chains were mainly generated outside of lamellar stacks due to the confined space. As such, d_1 does not obviously change even though GD continuously increases.[20, 23] This also shows that d_1 of AEMs at 80% RH is slightly larger than that of the corresponding dry AEMs because of the incorporated water, but the deviation of d_1 between these two states is much smaller than between dry AEMs and AEMs equilibrated in water as previously reported,[20] due to the lower WU of AEMs at 80% RH compared to the case in water.

For the SAXS profiles recorded at GD of 30%, 48%, 91% and 108% in this study, and the SANS profiles recorded at GD of 91% in our previous study,[20] apart from the impact on the lamellar structure, the effects of grafting, alkylation and swelling do not induce additional significant changes in the polymer morphologies on the length scale of a few to tens of nanometers, *i.e.* $q < 2$ nm^{-1}.

Region 2. Similar to Figure 3, SAXS profiles of AEMs in the dry state and at 80% RH (Figure 8 and Figure S4) clearly show two scattering maxima in Region 2: the amorphous ETFE halo at ~ 12.0 nm^{-1} and the ion-related peak at approximately q = 5 nm^{-1}. The position of the amorphous ETFE halo is not affected by GD, whereas the intensity decreases with increasing GD due to the decrease of the volume fraction of ETFE amorphous regions by incorporating grafts. The ion-related peak can be fitted well by Eq. (6) at q = 4–9 nm^{-1}, as shown in Figure 8(b) and Figure S4(b) in red lines. Thus, d_{ion} of AEMs at both dry and 80% RH conditions can be estimated and plotted as a function of GD in Figure 9(b), showing that d_{ion} is ~0.9 nm in the dry state and ~1.1 nm at 80% RH, both of which are GD-independent.

To understand the effects of GD on the hydration level of the cations, n_w was calculated for all AEMs at 80% RH using Eq. (7) and plotted as a function of GD in Figure 9(c). The n_w of AEMs varies from 3.9 to 5.3. The n_w values are quite lower than those of PEMs under identical conditions. Such small n_w values together with the small d_{ion} values mentioned above

support the image of disconnected ion-channels as shown in Figure 5(a) at RH < 80%. Namely, as GD increases, the total volume of the grafting (hydrophilic) regions increases without any influence on the ionic structure in the conducting regions of these AEMs, as illustrated in Figure 10.

According to this model, the characteristic scattering intensity of the ion-related peak, defined by $A = I_{m,ion} q_{m,ion}^2$ should be given by Eq. (8)[49]

$$A = \Delta\rho^2 n_{ion} V_{ion}^2 \quad (8)$$

where $\Delta\rho$ is the scattering contrast between the ion-pair and the polymer matrix, n_{ion} is the number of ion-pairs, and V_{ion} is the volume of one ion-pair. Since the numbers of the unit graft chains are linearly related to those of the ion-pairs in all AEMs, it is rational to assume that all AEMs have the same $\Delta\rho$ and V_{ion}. Thus, Eq. (8) can be simplified to $A \propto n_{ion}$. It is known that grafts are the only polymer component containing ions, meaning n_{ion} is proportional to ϕ_{graft}, leading to the assumption $A \propto \phi_{graft}$. Thus, we plotted A as a function of ϕ_{graft} for all AEMs with different GDs at both dry and 80% RH conditions as shown in Figure 11, indicating good linear correlation between the two. Note that the plots of A vs ϕ_{graft} for AEM91 at different RH values also overlap in the same region (shown with filled triangles), revealing that the linearity between A and n_{ion} ($=\phi_{graft}$) in Eq. (8) is universally independent of GD and the hydration level.

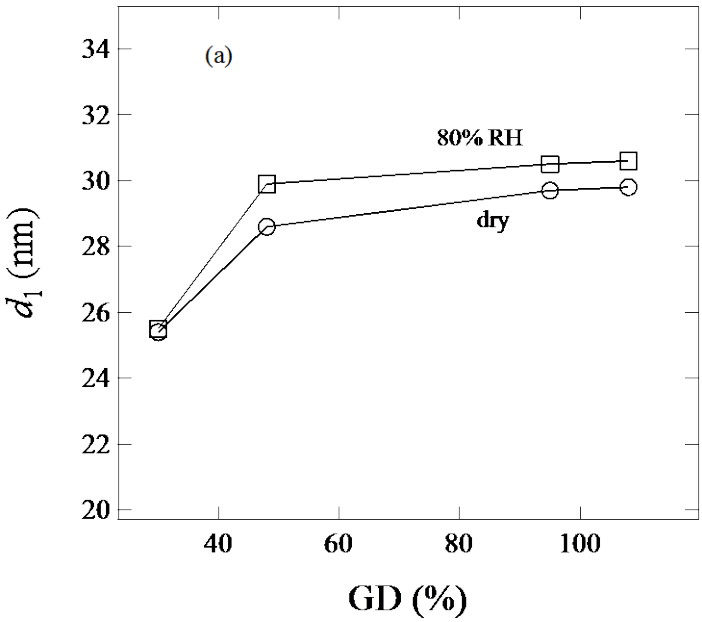
(a)
80% RH
dry
d_1 (nm)
GD (%)
34
32
30
28
26
24
22
20
40
60
80
100

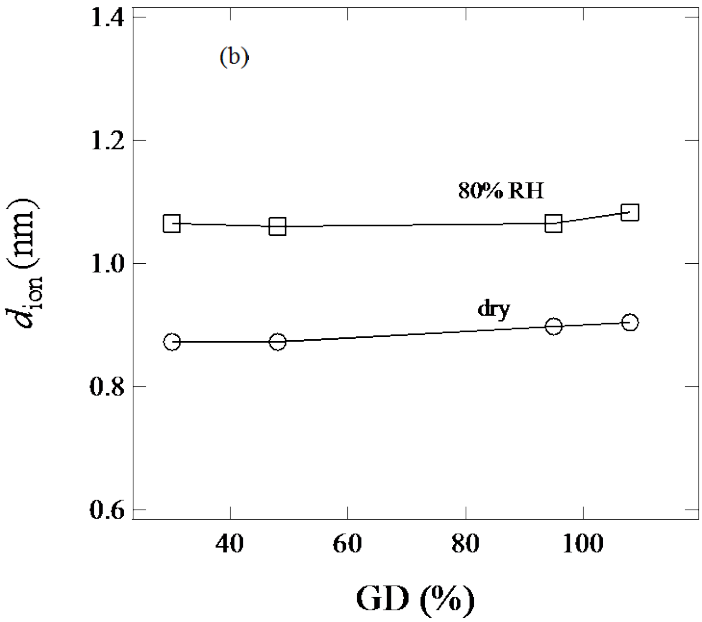
(b)
80% RH
dry
d_{ion} (nm)
GD (%)
1.4
1.2
1.0
0.8
0.6
40
60
80
100

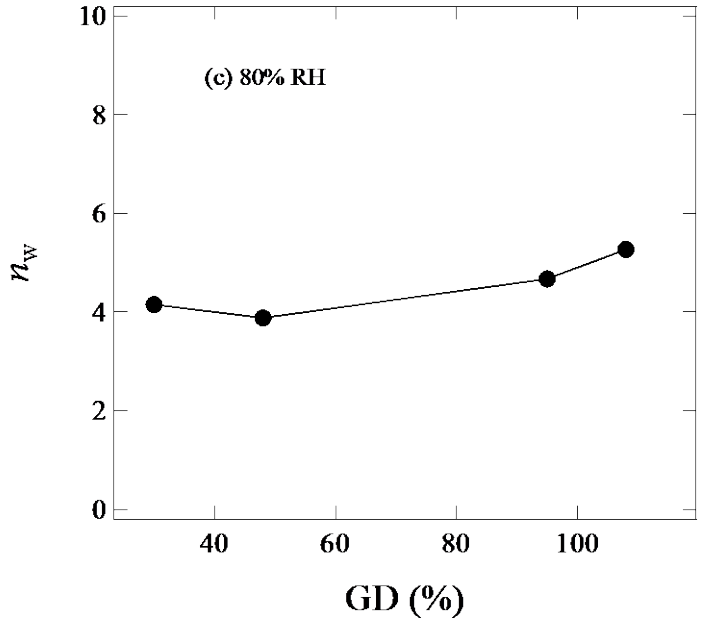

Figure 9 GD dependence of (a) d_1 and (b) d_{ion} for all AEMs at dry and 80% RH states; (c) n_w for all AEMs at 80% RH.

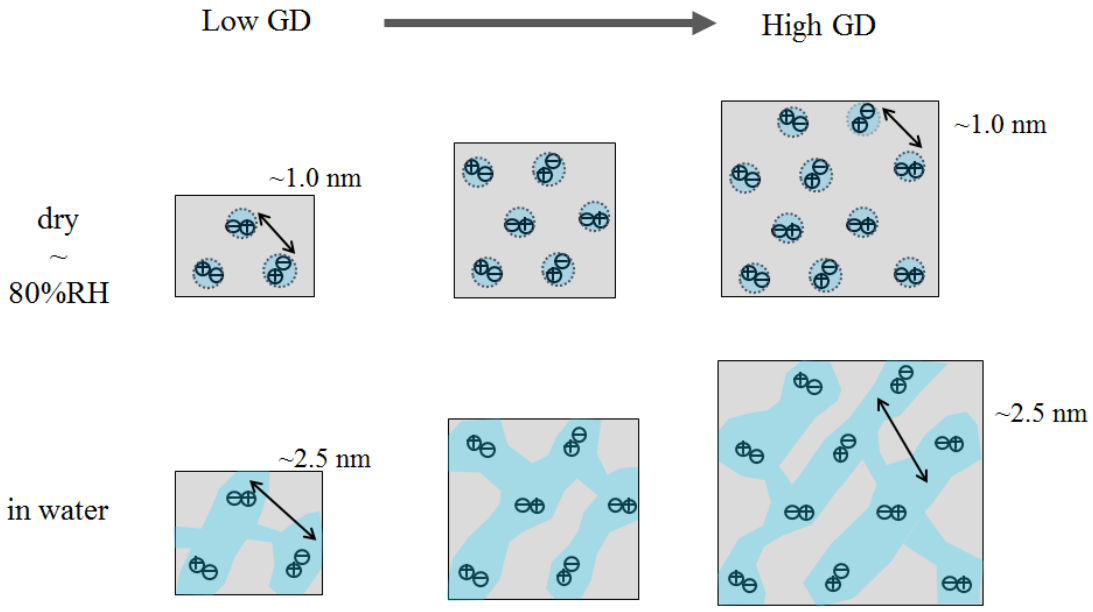

Figure 10 Schematic illustration of the grafting degree and hydration level effects on the ionic structure of ion channels in AEMs.

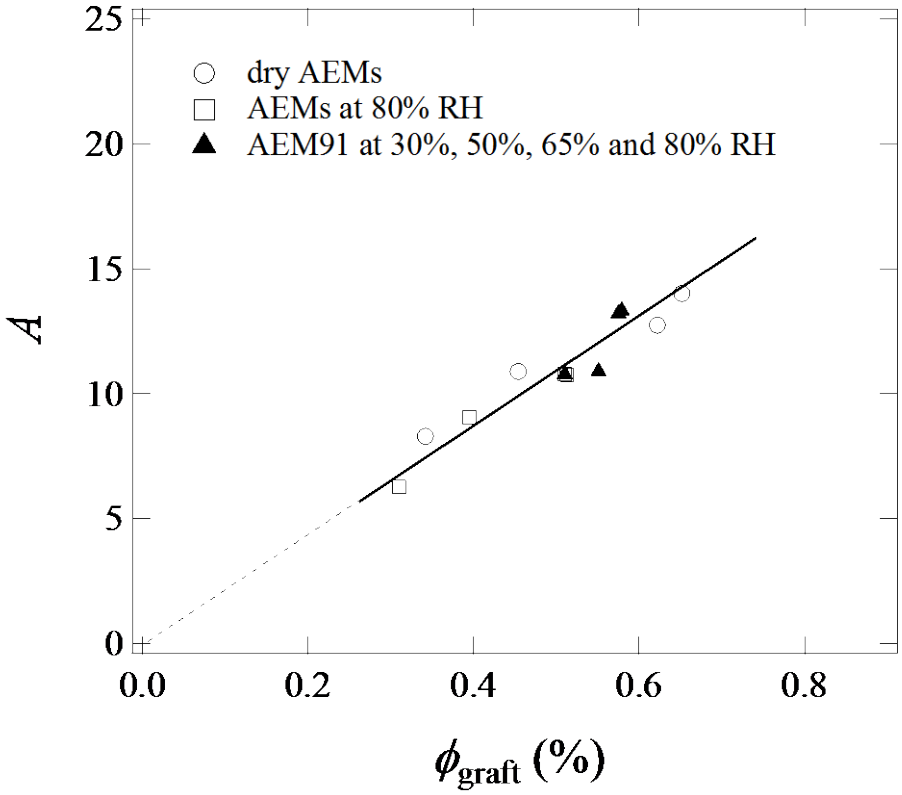

Figure 11 Characteristic scattering intensity A ($=I_{m,ion}q_{m,ion}^2$) as a function of ϕ_{graft} for AEMs with different GDs at dry (hollow circles) and equilibrated at 80% RH (hollow squares), and AEM91 equilibrated at different RH (sold triangles).

Similar to the case of Figure 5, we also examined the Arrhenius behavior of conductivities for AEMs with different GDs at 80% RH from 25–80 °C in Figure S6 in the supporting information. As with Figure S3, E_a values of the anion transport were estimated by Eq. (5), and are plotted in Figure 12. E_a within T-range 1 is slightly larger than within T-range 2, and E_a was constant over the entire GD range. These results suggest the same anion transport mechanisms for all AEMs at a given 80% RH, also verifying the ionic structure obtained by SAXS under the same RH condition. Note that the similar phenomenon is commonly observed at other RH conditions, *i.e.* 50% RH and liquid water as shown in Figure S7, further confirming the patterns illustrated in Figure 10.

The changes in E_a shown in Figures 6 and 12 are in good agreement with the change in the

ionic structure shown in Figures 5 and 10, indicating that ionic structure is the key factor in manipulating the conductivity. The ionic structure does not change with GD at a given RH, but does change with RH, and consequentially E_a of anion transport behaves the same way.

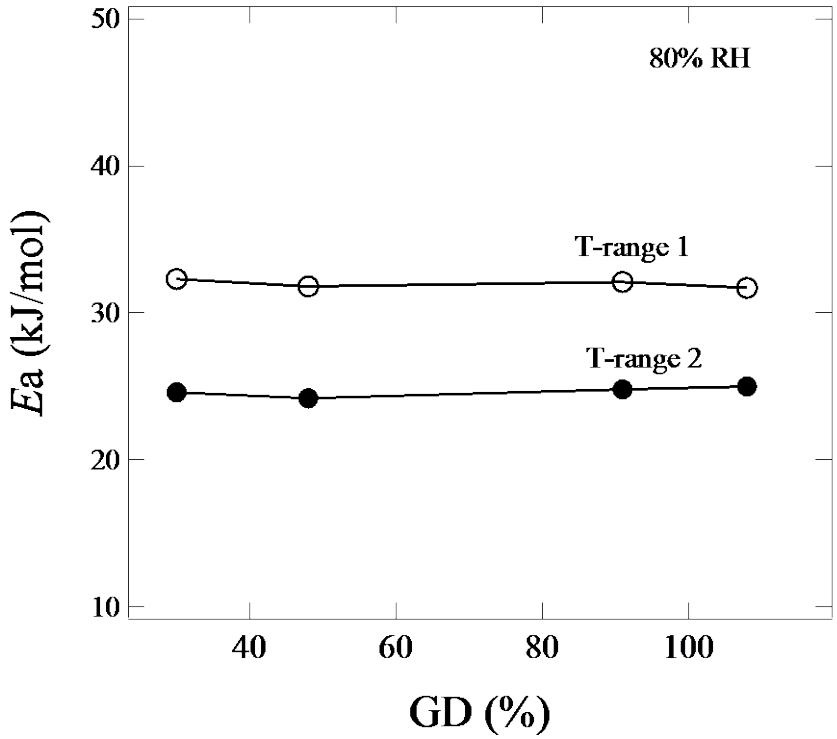

Figure 12 GD dependence of E_a for AEMs with different GDs at 80% RH.

III-4, Correlations between the conductivity, hydration level and morphology of AEMs. Unlike most ion-containing membranes such as Nafion, where the presence of ionic clusters results from electrostatic interactions, we have found that these new graft-type AEMs have dissociated ion-pairs in the hydrophilic domains, resulting in much smaller d_{ion} compared with the mean distance between two ionic clusters, which generally decreases counter-ion condensation[59–61] and promotes anion transport. We have also found that hydration level influences the conductivity of these grafted AEMs severely. Namely, at RH < 80%, σ changes steadily with RH, while in water, σ increases more significantly. The key reason for this phenomenon is the change in the hydrophilic domains or ion-channels from disconnected to well-connected. Such a sensitive RH dependence of the ionic structure of the ion-channels is

expected to contribute to the low power generation of most AEMs reported to date. The reduction reaction at the cathode ($O_2 + H_2O \rightarrow OH^-$) is subject to the lack of water, meaning that the possible disconnection of ion-channels in the AEM at the zones near the cathode seriously decreases the anion transport.

IV. Conclusions

We have continued the study of the hierarchical structure in previously-developed AEMs[20] composed of poly(dimethyl-vinylimidazole-co-styrene) copolymer chains grafted onto ETFE films via a radiation-induced grafting method, and have investigated the ionic structure of ion-channels in these AEMs by SAXS. Owing to the enhanced scattering contrast and expanded *q*-range, the SAXS results in this work elucidate the ionic structure and its impact on the conducting properties. Dissociated ion-pairs are distributed in the ion-channels, and at RH < 80%, ion-channels are disconnected, leading to low conductivity, while in liquid water, ion channels are well-connected, significantly increasing the conductivity. This structural model explains the low power generation of current AEMs in the literature.

Acknowledgments.

This work was partially supported by the Advanced Low Carbon Technology Research and Development Program (ALCA) from the Japan Science and Technology Agency (JST).

References and Notes.

1. A. Serov, C. Kwak, *Appl. Catal. B: Environ.*, 2010, **98**, 1-9.
2. K. Asazawa, K. Yamada, H. Tanaka, A. Oka, M. Taniguchi, T. Kobayashi, *Angew. Chem., Int. Ed.*, 2007, **46**, 8024-8027.
3. J. R. Varcoe, R. C. T. Slade, *Fuel Cells*, 2005, **5**, 187-200.
4. M. A. Hickner, A. M. Herring, E. B. Coughlin, *J. Polym. Sci., Part B: Polym. Phys.*, 2013, **51**, 1727-1735.
5. J. R. Varcoe, P. Atanassov, D. R. Dekel, A. M. Herring, M. A. Hickner, P. A. Kohl, A. R. Kucernak, W. E. Mustain, K. Nijmeijer, K. Scott, T. Xu, L. Zhuang, *Energy Environ. Sci.*, 2014, **7**, 3135-3191.
6. G. Couture, A. Alaaeddine, F. Boschet, B. Ameduri, *Prog. Polym. Sci.*, 2011, **36**, 1521-1557.
7. G. Merle, M. Wessling, K. Nijmeijer, *J. Membr. Sci.*, 2011, **377**, 1-35.
8. W. Vielstich, A. Lamm, H. Gasteiger, *Handbook of Fuel Cells: Fundamentals, Technology, Applications*; John Wiley: 2004.
9. S.G. Chalk, J. F. Miller, F. W. Wagner, *J. Power Sources*, 2000, **86**, 40-51.
10. G. Cacciola, V. Antonucci, S. Freni, *J. Power Sources*, 2001, **100**, 67-79.
11. P. Costamagna, S. Srinivasan, *J. Power Sources*, 2001, **102**, 253-269.
12. A. F. Ghenciu, *Curr. Opin. Solid State Mater. Sci.*, 2002, **6**, 389-399.
13. S. Gamburzev, A. J. Appleby, *J. Power Sources*, 2002, **107**, 5-12.
14. V. Mehta, J. S. Cooper, *J. Power Sources*, 2003, **114**, 32-53.
15. H. A. Gasteiger, J. E. Panels, *J. Power Sources*, 2004, **127**, 162-171.
16. M. Z. Jacobson, W. G. Colella, D. M. Golden, *Science*, 2005, **308**, 1901-1905.
17. J. H. Wee, *Renewable & Sustainable Energy Reviews*, 2007, **11**, 1720-1738.
18. Y. Wang, K. Chen, J. Mishler, S. C. Cho, X. C. Adroher, *Appl. Energy*, 2011, **88**, 981-1007.
19. M. R. Hibbs, M. A. Hickner, T. M. Alam, S. K. Mclntyre, H. Fujimoto, C. J. Cornelius, *Chem. Mater.*, 2008, **20**, 2566-2573.

20. Y. Zhao, K. Yoshimura, H. Shishitani, S. Yamaguchi, H. Tanaka, S. Koizumi, N. Szekely, A. Radulescu, D. Richter, Y. Maekawa, *Soft Matter*, 2016, **12**, 1567-1578.
21. H. Iwase, S. Sawada, T. Yamaki, S. Koizumi, M. Ohnuma, Y. Maekawa, *Macromolecules*, 2012, **45**, 9121-9127.
22. I H. Iwase, S. Sawada, T. Yamaki, Y. Maekawa, S. Koizumi, *Inter. J. Polym. Sci*., 2011, **7**, 301807.
23. T. D. Tap, S. Sawada, K. Hasegawa, Y. Yoshimura, M. Oba, M. Ohnuma, Y. Katsumura, Y. Maekawa, *Macromolecules*, 2014, **47**, 2373-.
24. N. Li, T. Yan, Z. Li, T. T. Albrecht, W. H. Binder, *Energy Environ. Sci.*, 2012, **5**, 7888-7892.
25. N. Li, Q. Zhang, C. Wang, Y.M. Lee, M. D. Guiver, *Macromolecules*, 2012, **45**, 2411-2419.
26. F. Zhang, H. Zhang, C. Qu, *J. Mater. Chem.*, 2011, **21**, 12744-12752.
27. H. Zhang, P. Shen, *Chem. Rev.*, 2012, **112**, 2780-2832.
28. K. Mortensen, U. Gasser, S. A. Guersel, G. G. Scherer, *J. Polym Sci. Polym. Phys. Ed.*, 2008, **46**, 1660-1668.
29. M. M. Nasef, E. A. Hegazy, *Prog. Polym. Sci*., 2004, **29**, 499-561.
30. J. M. Song, B. S. Ko, J.Y. Sohn, Y. C. Nho, J. Shin, *Rad. Phys. Chem.*, 2014, **97**, 374-380.
31. K. Yoshimura, H. Koshikawa, T. Yamaki, H. Shishitani, K. Yamamoto, S. Yamaguchi, H. Tanaka, Y. Maekawa, *J. Electrochem. Soc.*, 2014, **161**, F889-F893.
32. H. Long, B. Pivovar, *J. Phys. Chem. C*, 2004, 118, 9880-9888.
33. W. Q. Wang, W. J. Liu, G. J. Tudryn, R. H. Colby, K. I. Winey, *Macromolecules*, 2010, **43**, 4223-4229.
34. W. Y. Hsu; T. D. Gierke, *J. Membr. Sci.*, 1983, **13**, 307.
35. S. Y. Kim, M. J. Park, N. P. Balsara, A. Jackson, *Macromolecules*, 2010, **43**, 8128-8135.
36. A. Kusoglu, M. A. Modestino, A. Hexemer, R. A. Segalman, A. Z. Weber, *ACS Macro Lett.*, 2012, **1**, 33-36.
37. M. E. Seitz, C. D. Chan, K. L. Opper, T. W. Baughman, K. B. Wagener, K. I. Winey, *J. Am.*

Chem. Soc., 2010, **132**, 8165-8174.

38. D. J. Yarusso, S. L. Cooper, *Macromolecules*, 1983, **16**, 1871-1880.
39. S. P. Ertem, T.H. Tsai, M. M. Donahue, W. Zhang, H. Sarode, Y. Liu, S. Seifert, A. M. Herring, E. B. Coughlin, *Macromolecules*, 2016, **49**, 153-161.
40. G. S. Manning, *J. Chem. Phys.*, 1969, **51**, 924.
41. H. Koshikawa, K. Yoshimura, W. Ainnananchi, T. Yamaki, M. Asano, K. Yamamoto, S. Yamaguchi, H. Tanaka, Y. Maekawa, *Macromol. Chem. Phys.*, 2013, **214**, 1756-1762.
42. G. D. Wignal, F. S. Bates, *J. Appl. Cryst.*, 1987, **20**, 28-40.
43. D. Stoica, F. Alloin, S. Marais, D. Langevin, C. Chappey and P. Judeinstein, *J. Phys. Chem. B*, 2008, **112**, 12338-12346.
44. J. R. Varcoe, *Phys. Chem. Chem. Phys.*, 2007, **9**, 1479-1486.
45. Y. S. Li; T.S. Zhao, W.W. Yang Measurements of water uptake and transport properties in anion-exchange membranes, *Int J Hydrogen Energy*, 2010, **35**, 5656-5665.
46. X. Wu, X. Wang, G. He, J. Benziger, *J. Polym. Sci. B: Polym. Phys.*, 2011, **49**, 1437–1445.
47. P. Schroeder, *Z. Phys. Chem.*, 1903, **45**, 75-117.
48. V. Sproll, G. Nagy, U. Gasser, J. P. Embs, M. Obiols-Rabasa, T. J. Schmidt, L. Gubler, S. Balog, *Macromolecules*, 2016, **49**, 4253-4264.
49. R. J. Roe, *Methods of X-ray and neutron scattering in polymer science*, Oxford Uni. Press, New York, 2000.
50. D. H. Powell, A. C. Barnes, J. E. Enderby, G. W. Neilson, P. S. Salmon, *Faraday Discuss. Chem. Soc.*, 1988, **85**, 137-146.
51. T. P. Pandey, H. N. Sarode, Y. Yang, Y. Yang, K. Vezzu, V. D. Noto, S. Seifert, D. M. Knauss, M. W. Liberatore, A. M. Herring, *J. Electrchem. Soc.*, 2016, **163**, H513-H520.
52. M. Cappadonia, J. W. Erning, S. M. S. Niaki, U. Stimming, *Solid State Ionics*, 1995, **77**, 65-69.
53. T. P. Pandey, A. M. Maes, H. N. Sarode, B. D. Peters, S. Lavina, K. Vezzu, Y. Yang, S. D.

Poynton, J. R. Varcoe, S. Seifert, M. W. Liberatore, V. D. Noto, A. M. Herring, *Phys. Chem. Chem. Phys.*, 2015, **17**, 4367-4378.

54. R. C. T. Slade, J. R. Varcoe, *Solid State Ionics*, 2005, **176**, 585–597.
55. Y. Li, Y. Liu, A. M. Savage, F. L. Beyer, S. Seifert, A. M. Herring, D. M. Knauss, *Macromolecules*, 2015, **48**, 6523-6533.
56. A. Amel, N. Gavish, L. Zhu, D. R. Dekel, M. A. Hickner, Y. Ein-Eli, *J. Membr. Sci.*, 2016, **514**, 125-134.
57. Y.L.S. Tse, H. N. Sarode, G. E. Lindberg, T. A. Witten, Y. Yang, A. M. Herring, *J. Phys. Chem. C*, 2013, **118**, 845-853.
58. Y.L.S. Tse, G. A. Voth, T. A. Witten, *J. Chem. Phys.*, 2015, **142**, 184905.
59. K. M. Beers, N. P. Balsara, *ACS Macro Lett.*, 2012, **1**, 1155-1160.
60. K. M. Beers, Jr. D. T. Hallinan, X. Wang, J. A. Pople, N. P. Balsara, *Macromolecules*, 2011, **44**, 8866-8870.
61. A. L. Rollet, O. Diat, G. Gebel, *J. Phys. Chem. B*, 2002, **106**, 3033-3036.

Figure captions

Scheme 1 Preparation procedures for AEMs by radiation-induced grafting of 2-methyl-1-vinylimidazole and styrene into ETFE films, followed by *N*-alkylation with methyliodide, and the molecular structure of the AEMs used in this study.

Figure 1 RH dependence of (a) WU and (b) σ of AEM91 at room temperature.

Figure 2 GD dependence of (a) WU and (b) σ of AEMs equilibrated at 80% RH and in liquid water at room temperature.

Figure 3 SAXS profiles measured for AEM91 equilibrated at RH of 0% (black), 30% (green), 50% (pink), 65% (yellow), and 80% (blue) at room temperature. The vertical broken line indicates the boundary between Region 1 and Region 2.

Figure 4 RH dependence of (a) d_1, (b) d_{ion}, and (c) n_w of AEM91. Note that the points in water are marked by arrows, where data in (a) and (b) are taken from the SANS results in Ref. 20, and the one in (b) is the correlation length between two ion channels.

Figure 5 Schematic illustrations of the ionic structure of ion channels in AEM91 (a) at RH < 80% and (b) in water.

Figure 6 RH dependence of E_a for AEM91.

Figure 7 σ as a function of n_w/d_{ion} for AEM91 at RH < 80%. The threshold value of n_w/d_{ion} (~1.78) for $\sigma = 0$ is marked by the arrow.

Figure 8 SAXS profiles measured for AEMs with different GDs in the dry state at room temperature (a) in absolute intensity units and (b) in arbitrary units derived by vertically shifting profiles shown in part (a) to avoid overlapping. The best-fitted theoretical profile across the ion-related peak from Eq. (6) for each measured scattering profile is shown using red lines. The vertical broken lines in both parts indicate the boundary between Region 1 and Region 2.

Figure 9 GD dependence of (a) d_1 and (b) d_{ion} for all AEMs at dry and 80% RH states; (c) n_w for all AEMs at 80% RH.

Figure 10 Schematic illustration of the grafting degree and hydration level effects on the ionic structure of ion channels in AEMs.

Figure 11 Characteristic scattering intensity A ($=I_{m,ion}q_{m,ion}^2$) as a function of ϕ_{graft} for AEMs with different GDs at dry (hollow circles) and equilibrated at 80% RH (hollow squares), and AEM91 equilibrated at different RH (sold triangles).

Figure 12 GD dependence of E_a for AEMs with different GDs at 80% RH.

Table 1 Characteristics of AEMs at dry, equilibrated at different RH and water at 25 °C.

AEM	*GD* (%)	*IEC* (mmol/g)	Hydration condition	d_{ion} (nm)	σ (mS/cm)	*WU* (%)	*SR* (%)	ϕ_{graft}	*E*a (kJ/mol) T-range1	T-range2
AEM30	30	0.95	water	-	6.6	23.0	25.7	-	-	
			80%RH	1.06	0.9	7.1	4.3	0.310	32.3±2.0	24.6±0.1
			Dry	0.87	-	-	-	0.342	-	
AEM48	48	1.56	Water	-	12.3	40.4	43.1	-	-	
			80%RH	1.06	1.6	10.9	6.7	0.395	31.8±0.6	24.2±0.9
			dry	0.87	-	-	-	0.454	-	
AEM91	91	1.82	water	2.5*	21	60.2	40.2	-	19.7±0.2	13.8±0.8
			80%RH	1.06	4.3	17.5	16.4	0.51	32.1±2.3	24.8±0.7
			65%RH	0.97	1.1	10.0	9.0	0.551	37.4±1.4	30.1±0.6
			50%RH	0.93	0.3	6.5	6.2	0.575	40.6±1.5	33.6±0.3
			30%RH	0.91	0.1	5.9	6.1	0.579	-	
			dry	0.89	-	-	-	0.622	-	
AEM108	108	2.32	water	-	24	70.1	47.4	-	-	
			80%RH	1.08	5.2	22.0	18.9	0.513	31.7±1.4	25.0±1.4
			dry	0.90	-	-	-	0.652	-	

* Correlation length between two ion channels

Imidazolium-Based Anion Exchange Membranes for Alkaline Anion Fuel Cells: (2) Elucidation of the Ionic Structure and its Impact on the Ion Conductivity

Kimio Yoshimura,[1] Yue Zhao,[1,*] Shin Hasegawa,[1] Akihiro Hiroki,[1] Yoshihiro Kishiyama,[2] Hideyuki Shishitani,[2] Susumu Yamaguchi,[2] Hirohisa Tanaka,[2] Satoshi Koizumi,[3] Marie-Sousai Appavou,[4] Aurel Radulescu,[4] Dieter Richter,[5] Yasunari Maekawa[1,*]

[1]*Department of Advanced Functional Materials Research, Takasaki Advanced Radiation Science Institute, National Institutes for Quantum and Radiological Science and Technology (QST), Watanuki-machi 1233, Takasaki, Gunma, 370-1292, Japan*

[2]*Daihatsu Motor Co., Ltd., Ryuo Gamo, Shiga 520-2593, Japan*

[3]*Department of Engineering, Ibaraki University, Hitachi 316-8511, Japan*

[4]*Forschungszentrum Jülich GmbH, Jülich Centre for Neutron Science @ MLZ, Lichtenbergstraße 1, D-85747 Garching, Germany*

[5]*Jülich Centre for Neutron Science & Institute for Complex Systems, Forschungszentrum Jülich GmbH, D-52425 Jülich, Germany*

Table of Contents Graphic